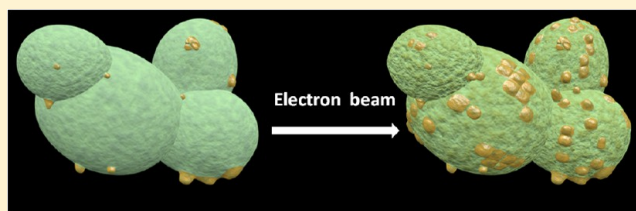


Experimental and Theoretical Study on the Structure, Optical Properties, and Growth of Metallic Silver Nanostructures in Ag_3PO_4 G. Botelho,[†] J. C. Sczancoski,[‡] J. Andres,[§] L. Gracia,^{*,§} and E. Longo[‡][†]INCTMN-UFSCar, Universidade Federal de São Carlos, P.O. Box 676, 13565-905 São Carlos, SP, Brazil[‡]INCTMN-UNESP, Universidade Estadual Paulista, P.O. Box 355, CEP. 14801-907 Araraquara, SP, Brazil[§]Departament de Química Física i Analítica, Universitat Jaume I, 12071 Castelló de la Plana, Spain

S Supporting Information

ABSTRACT: Theoretical and experimental studies were performed on the structure, optical properties, and growth of silver nanostructures in silver phosphate (Ag_3PO_4). This material was synthesized by the coprecipitation method and processed in a microwave-assisted hydrothermal system at 150 °C for different times. The structural behavior was analyzed by means of X-ray diffraction, Rietveld refinement, and Raman spectroscopy. Field emission gun scanning electron microscopy as well as transmission electron microscopy revealed the presence of irregular spherical-like Ag_3PO_4 microparticles; metallic silver nanostructures were found on their surfaces. The growth processes of Ag nanostructures when irradiated with an electron beam were explained by theoretical calculations. First-principles calculations, within a quantum theory of atoms in molecules framework, have been carried out to provide deeper insight and understanding of the observed nucleation and early evolution of Ag nanoparticles on Ag_3PO_4 crystals, driven by an accelerated electron beam from an electronic microscope under high vacuum. The Ag nucleation and formation is a result of structural and electronic changes of the AgO_4 tetrahedral cluster as a constituent building block of Ag_3PO_4 , consistent with Ag metallic formation. The optical properties were investigated by ultraviolet–visible spectroscopy and photoluminescence (PL) measurements at room temperature. PL properties of this phosphate were explained by the recombination phenomenon of electron–hole pairs via cluster-to-cluster charge transfer.



1. INTRODUCTION

In nature, silver phosphate (Ag_3PO_4) crystallizes in a body-centered cubic structure with space group $P43n$.¹ This material has received considerable attention from the scientific community because of its photooxidative applications.^{2–15} To improve these physicochemical properties, heterostructures consisting of Ag_3PO_4 and other materials (TiO_2 ,^{5,16,17} Ag ,^{18–21} Fe_2O_3 ,²² $\text{AgX}/\text{Ag}_3\text{PO}_4$ ($X = \text{Cl}, \text{Br}, \text{I}$),²³ C_3N_4 – Ag_3PO_4 ,²⁴ and graphene¹⁴), also have been studied. One of the first publications on the photooxidative property of Ag_3PO_4 was performed by Tennakone et al.²⁵ in 1988, who synthesized this phosphate by the coprecipitation (CP) route and analyzed its potential to photogenerate both H_2 and O_2 from water.

In terms of chemical synthesis techniques, the bottom-up approach is considered a good strategy for the preparation of a wide variety of ceramic oxides with controlled particle shapes and sizes (nano-, meso-, or microscale).^{26,27} The most popular bottom-up approaches employed in materials science are CP and conventional hydrothermal processing.^{5,8,28–30} Particularly, Komarneni et al.^{31–33} introduced the hydrothermal systems by using microwave radiation instead of the typical electric heaters as an energy source. This new apparatus was called microwave–hydrothermal, which allowed the synthesis of several inorganic materials.^{29–31} Besides producing an efficient internal heating of the aqueous solution simultaneously and uniformly, the microwave radiation route offers high heating rates,

selective heating, morphology control, and higher yields.^{29,32} These advantages of the microwaves involve the physics concepts of dipolar polarization and ionic conduction.³⁴ In dipolar polarization, the permanent or induced dipoles of the molecules tend to align with the oscillating microwave electric field. The energy arising from the cyclic motion of the molecules is converted into thermal energy. If a molecule is ionic, then the electric field component of the microwave radiation moves the ions back and forth through the sample. This continuous movement generates thermal energy. However, scientific studies on the preparation of Ag_3PO_4 by this method are not found in the literature.

Recently, our research group has reported that ceramic oxides containing Ag in their structural composition show nucleation and growth processes of metallic Ag on their surfaces when exposed to an electron beam.^{35–38} Following that work, we used an electron beam to grow Ag nanoparticles from Ag_3PO_4 crystals using different periods of irradiation. This paper reports a theoretical and experimental study on the structural, morphological, and optical properties of Ag_3PO_4 powders synthesized by the CP route and processed in a microwave-assisted hydrothermal (MAH) system at 150 °C for

Received: December 4, 2014

Revised: February 24, 2015

Published: February 25, 2015



different times. These powders were structurally characterized by means of X-ray diffraction (XRD), Rietveld refinements, and micro-Raman (MR) spectroscopy.

Ultraviolet–visible (UV–vis) absorption spectroscopy and photoluminescence (PL) measurements at room temperature were performed to verify the correlation between optical properties and structural order–disorder effects. First-principles density functional theory (DFT) calculations were carried out to understand the physical phenomena involved in the growth stages of metallic Ag nanostructures on the surface of Ag_3PO_4 microparticles.

The paper is organized as follows: section 2 describes the experimental procedure, and section 3 contains the results together with a discussion concerning the structure and optical properties. In addition, based on the experimental results, a plausible mechanism to find a relationship between optical properties and order–disorder effects is proposed. Comprehensive and combined experimental and theoretical results are reported to understand the observed nucleation and early evolution of Ag nanoparticles on Ag_3PO_4 crystals when driven by an accelerated electron beam from an electron microscope under high vacuum. Finally, the main conclusions are summarized in section 4.

2. EXPERIMENTAL PROCEDURE

2.1. Synthesis. Ag_3PO_4 powders were synthesized by the CP method and processed in a MAH system at 150 °C for different times. Silver nitrate [AgNO_3] (99.8%, Vetec) and diammonium hydrogen phosphate [$(\text{NH}_4)_2\text{HPO}_4$] (98.6%, J.T. Baker) were used as starting precursors. Initially, $(\text{NH}_4)_2\text{HPO}_4$ (1×10^{-3} mol) and AgNO_3 (3×10^{-3} mol) precursors were separately dissolved in two beakers containing 25 and 75 mL of deionized water, respectively. Both solutions were quickly mixed, promoting the instantaneous formation of solid Ag_3PO_4 precipitates (yellow coloration). This resulting mixture was transferred to a Teflon autoclave, which was sealed and placed inside the adapted MAH apparatus.³⁹ The hydrothermal treatments were performed at 150 °C for 8, 16, and 32 min, respectively. The pressure inside the autoclave stabilized at 4 atm. After being processed, the obtained suspension was naturally cooled to room temperature, washed with deionized water, and centrifuged several times to remove byproducts formed during the reaction. Finally, the collected powders were dried in a lab oven at 60 °C for several hours. The powder described as CP was not submitted to any hydrothermal treatment and therefore is considered the reference sample in our study.

2.2. Characterizations. Ag_3PO_4 powders were characterized by X-ray diffraction (XRD) using a D/Max-2500PC diffractometer (Rigaku, Japan) with Cu $K\alpha$ radiation ($\lambda = 1.5406$ Å) in the 2θ range from 10° to 80° and a scanning speed of 0.02°/min. The Rietveld routine adopted the 2θ range from 10° to 110° with a scanning speed of 0.01°/min. Micro-Raman spectroscopy was carried out using an iHR550 spectrometer (Horiba Jobin-Yvon, Japan) coupled to a CCD detector and an argon-ion laser (Melles Griot, United States) operating at 514.5 nm with maximum power of 200 mW. The spectra were measured in the range from 50 cm^{-1} to 1100 cm^{-1} . The ultraviolet–visible absorption spectra were taken using a Varian spectrophotometer model Cary 5G (United States) in diffuse reflection mode. The morphologies were analyzed using a Supra 35-VP field-emission scanning electron microscopy instrument (FE-SEM) (Carl Zeiss, Germany)

operated at 15 kV. The elemental composition analysis was performed by means of energy dispersive X-ray spectroscopy (EDS) using a FEI microscope model Tecnai G2 F20. PL spectra were measured with a Monospec 27 monochromator (Thermal Jarrel Ash, United States) coupled to a R446 photomultiplier (Hamamatsu Photonics, Japan). A krypton ion laser (Coherent Innova 200 K, United States) ($\lambda = 350$ nm) was used as an excitation source. The incident laser beam power on the sample was maintained at 15 mW. All experimental measurements were performed at room temperature.

2.3. Theoretical Calculations. First-principles total-energy calculations were carried out within the periodic density functional theory framework using the VASP program.^{40,41} The Kohn–Sham equations were solved using the screened hybrid functional proposed by Heyd, Scuseria, and Ernzerhof (HSE)^{42,43} in which a percentage of exact nonlocal Fock exchange is added to the Perdew, Burke, and Ernzerhof functional (30%), with a screening of 0.11 bohr^{−1} applied to partition the Coulomb potential into long-range and short-range terms, as is reported in some recent papers.^{44,45} The electron–ion interaction has been described by the projector augmented wave pseudopotentials.^{46,47} The plane-wave expansion was truncated at cutoff energy of 400 eV, and the Brillouin zones were sampled through Monkhorst–Pack special k-points grids that ensure geometrical and energetic convergence for the Ag_3PO_4 structures considered in this work. Vibrational frequency calculation has been performed at the Γ point within the harmonic approximation, and the dynamical matrix has been computed by numerical evaluation of the first derivative of the analytical atomic gradients. The keyword NELECT has been used to increase the number of electrons in the bulk structure, and all the crystal structures are optimized simultaneously on both the volume of the unit-cell and the atomic positions. The relationship between charge density topology and elements of molecular structure and bonding was noted by Bader.^{48,49} This relationship, Bader’s quantum theory of atoms in molecules (QTAIM),^{48,50,51} is now a well-recognized tool used to analyze electron density, describe interatomic interactions, and rationalize chemical bonding. The different strong and weak interactions between two atoms can be determined unequivocally from QTAIM calculations. According to the standard QTAIM framework, concepts such as (3, −1) bond critical points (BCPs), their respective bond paths (BPs), and $L(r) = -\nabla^2\rho(r)$ maps can be analyzed to reveal the nature of these interactions. A BCP serves as the origin of gradient lines of the electron density that define the interatomic surface or zero-flux surface which is a surface that unambiguously defines the boundary between two atoms and identifies the atomic basin, i.e., the electron density “belonging” to a specific atom.

3. RESULTS

3.1. Structural Order at Long Range. Figure 1 shows XRD patterns of Ag_3PO_4 powders synthesized by the CP route and subjected to the MAH treatment for different times.

Figure 1 shows that all diffractograms were perfectly indexed to the body-centered cubic structure with space group $P43n$, in good agreement with the Inorganic Crystal Structure Database (ICSD) No. 14000¹. The intense and well-defined peaks indicate all Ag_3PO_4 powders have a high degree of periodicity at long range. Diffraction peaks associated with secondary phases were not detected in the samples. If the amount of secondary

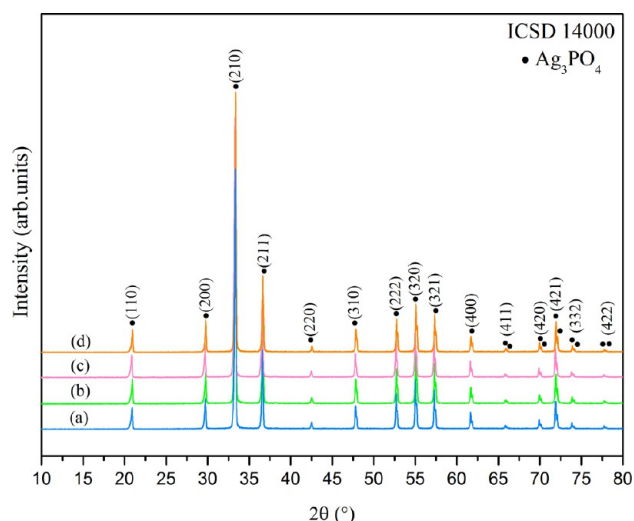


Figure 1. XRD patterns of Ag_3PO_4 powders obtained by the (a) CP route and processed in a MAH system for (b) 8 min, (c) 16 min, and (d) 32 min.

phase is below the detection limit imposed by the XRD analysis ($\approx 3\%$), it is impossible to confirm the existence of the metallic Ag phase in these samples. Therefore, other characterization techniques were employed in this study to obtain information on the structural organization of Ag_3PO_4 powders.

The Rietveld refinement method⁵² was used to calculate the lattice parameters and unit cell volumes of Ag_3PO_4 powders, thus analyzing the influences induced by the MAH processing.

The Rietveld refinements were performed using the general structure analysis system (GSAS) software package with the EXPGUI graphical interface.⁵³ The theoretical diffraction pattern was taken from ICSD No. 14000¹, which is based on the body-centered cubic structure with space group $P\bar{4}3n$. The refined parameters in these samples were scale factor; background fitting with the Chebyshev polynomial of the first kind; shift lattice constants; profile half-width parameters (u , v , w); isotropic thermal parameters; lattice parameters; strain anisotropy factor; preferential orientation; and atomic functional positions. The peak profile function was modeled using a convolution of the Thompson–Cox–Hastings pseudo-Voigt (pV-TCH) with the asymmetry function described by Finger, which accounts for the asymmetry due to axial divergence.⁵⁴ The Rietveld refinements of Ag_3PO_4 powders are shown in Figure 2, and their structural results in Table 1. More details are provided in Supporting Information (Table S1).

In this table, the statistic fitting parameters (R_{wp} , R_{p} , R_{Bragg} , and χ^2) indicate the quality of structural refinement data is acceptable. Significant changes in the lattice parameters and unit cell volumes were not found in these samples, which are in good agreement with those published in the literature.^{1,55} The lattice parameters and atomic positions obtained from Rietveld refinements were used as input data in the Crystal and Molecular Structure Visualization software to model the cubic Ag_3PO_4 structure (Figure 3) and estimate the bond angles and lengths associated with isolated $[\text{AgO}_4]$ and $[\text{PO}_4]$ clusters, as well as combined $[\text{AgO}_4]-[\text{AgO}_4]$ and $[\text{AgO}_4]-[\text{PO}_4]$ clusters (Supporting Information, Table S2).

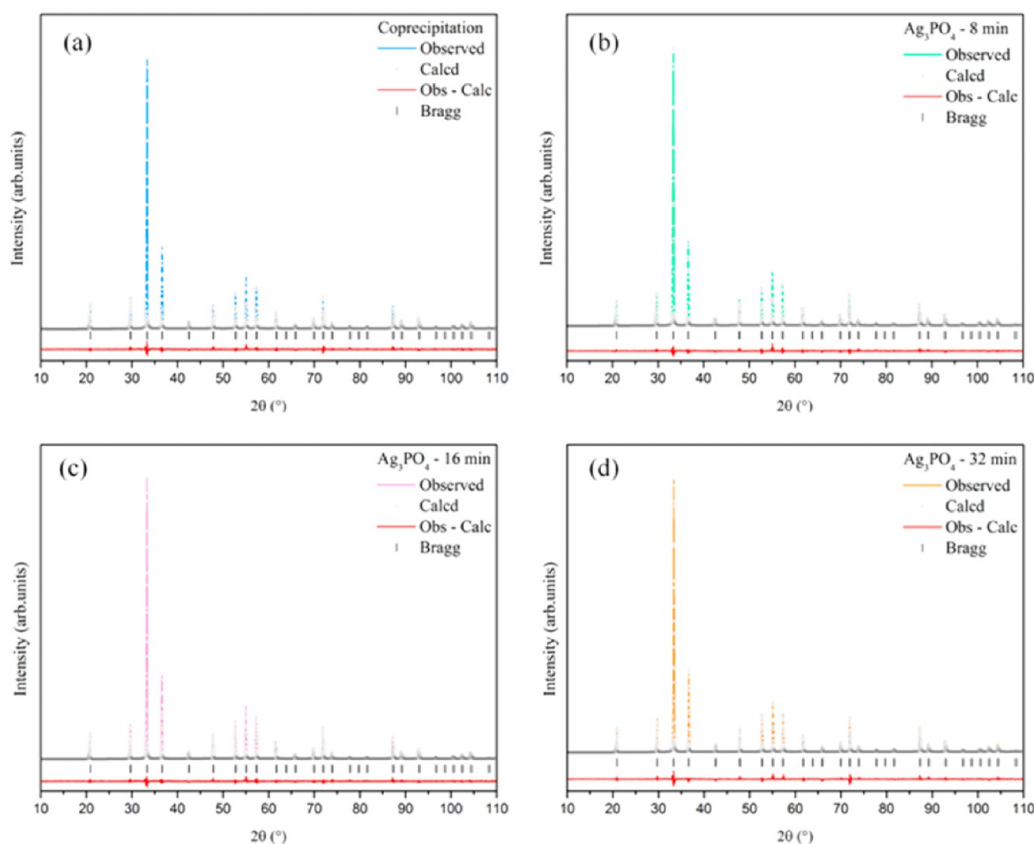
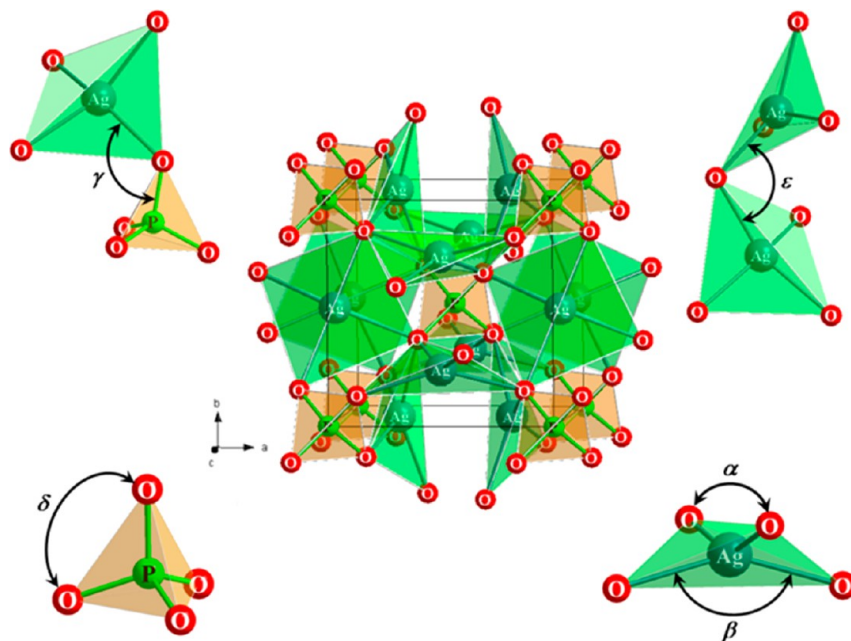


Figure 2. Rietveld refinement plots of Ag_3PO_4 powders obtained by the (a) CP route and processed in a MAH system for (b) 8 min, (c) 16 min, and (d) 32 min.

Table 1. Results Obtained from Rietveld Refinements of Ag_3PO_4 Powders

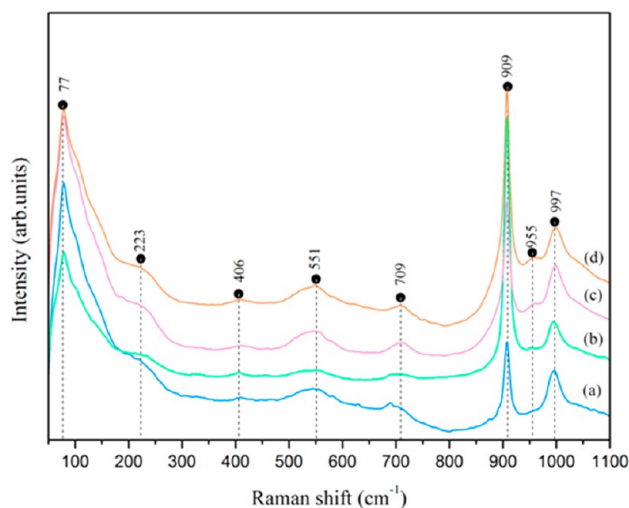
| sample | lattice parameter a (Å) | cell volume (Å) ³ | R_{Bragg} (%) | X^2 (%) | R_{wp} (%) | R_p (%) |
|--------------------------------------|---------------------------|------------------------------|------------------------|-----------|---------------------|-----------|
| Ag_3PO_4 , CP | 6.014(7) | 217.591(4) | 0.0498 | 1.2165 | 0.1438 | 0.0930 |
| Ag_3PO_4 , 8 min | 6.015(1) | 217.639(4) | 0.0562 | 1.1853 | 0.1422 | 0.0932 |
| Ag_3PO_4 , 16 min | 6.014(7) | 217.597(4) | 0.0485 | 1.1971 | 0.1397 | 0.0902 |
| Ag_3PO_4 , 32 min | 6.014(3) | 217.556(4) | 0.0723 | 1.2235 | 0.1613 | 0.1054 |
| Ag_3PO_4 , CIF 14000 | 6.026(5) | 218.82 | — | — | — | — |

Figure 3. Schematic representation of the cubic Ag_3PO_4 structure, illustrating both tetrahedral $[\text{AgO}_4]$ and $[\text{PO}_4]$ clusters.

In this modeled structure, both Ag and P atoms are coordinated to four oxygen (O) atoms, resulting in tetrahedral $[\text{AgO}_4]$ and $[\text{PO}_4]$ clusters. Each isolated $[\text{PO}_4]$ cluster is bonded to three neighboring $[\text{AgO}_4]$ clusters by means of O atoms. According to the qualitative results in Table S2, there are no considerable variations in the bond angles and lengths from one sample to another. The existence of two O–Ag–O bond angles (α , β) indicates the $[\text{AgO}_4]$ clusters are highly distorted in the lattice, as a consequence of the inductive effect caused by the high electronegativity of the regular $[\text{PO}_4]$ clusters.⁵⁵ Moreover, these results do not imply that the samples are free of surface and structural defects (cracks, pores, dislocations, grain boundaries, oxygen vacancies, etc.), which arise from the synthesis method as well as experimental conditions (temperature, heating rate, pH, liquid medium, concentration of precursors, microwave radiation, etc.) employed during the preparation of the material.

3.2. Structural Order at Short Range. Figure 4 shows Raman spectra of Ag_3PO_4 powders for which the relative positions of their experimental and theoretical vibrational bands are listed in Table 2.

Raman spectroscopy is considered a powerful technique for estimating the local structural order or short-range order of solids.^{56,57} In Figure 4, it was possible to experimentally identify eight Raman-active modes from a total of 18 theoretically predicted by first-principles calculations (Table 2). According to group-theory analysis, the allowed representation for each one of the corresponding Wyckoff positions of Ag_3PO_4 structure, in the $P43n$ space group, displays 18 Raman-active modes matching the following decomposition at the Γ point:

Figure 4. Raman spectra of Ag_3PO_4 powders synthesized by the (a) CP route and processed in a MAH system for (b) 8 min, (c) 16 min, and (d) 32 min.

$$\Gamma = 2A_1 + 4E + 12T_2$$

Some vibrational modes were not detected in these spectra because of overlapping bands and/or because of their low intensities. According to the literature,^{58–60} the band located at 909 cm^{-1} is attributed to symmetric stretching vibrations of $[\text{PO}_4]$ clusters, while the asymmetric stretching vibrations of this cluster were verified at 955 and 997 cm^{-1} . The bending

Table 2. Positions of Theoretical and Experimental Raman Modes of Ag_3PO_4

| Raman mode | theoretical | experimental | description |
|------------|-------------|--------------|---|
| T_2 | 32.43 | | |
| T_2 | 63.66 | | |
| T_2 | 82.97 | 77 | |
| T_2 | 88.47 | | |
| E | 89.72 | | rotation and translation of $[\text{PO}_4]$ units |
| E | 100.31 | | |
| T_2 | 142.23 | | |
| T_2 | 187.63 | | |
| T_2 | 212.54 | 223 | |
| T_2 | 250.29 | | |
| E | 407.44 | 406 | symmetric bending of the $[\text{PO}_4]$ |
| E | 458.05 | | symmetric bending of the $[\text{PO}_4]$ |
| T_2 | 550.74 | 551 | asymmetric bending of the $[\text{PO}_4]$ |
| T_2 | 552.53 | | asymmetric bending of the $[\text{PO}_4]$ |
| | | 709 | symmetric stretch of O–P–O bonds |
| A_1 | 908.68 | | symmetric stretch of O–P–O bonds |
| A_1 | 912.68 | 909 | symmetric stretch of O–P–O bonds |
| T_2 | 959.97 | 955 | asymmetric stretch of O–P–O bonds |
| T_2 | 995.91 | 997 | asymmetric stretch of O–P–O bonds |

vibration modes related to $[\text{PO}_4]$ clusters were found at 406 and 551 cm^{-1} .^{59,60} The band centered at 709 cm^{-1} is ascribed to symmetric stretching vibrations of P–O–P bonds.^{61–63} Theoretical calculations were not able to identify this vibrational band. However, some studies with symmetry T_d reported a band in this range as an example of combination mode Raman scattering ($T_2 + A_1$) that can sometimes appear in conjunction with the first-order normal modes.⁶⁴ Finally, bands detected at 77 and 223 cm^{-1} are in the range of the calculated modes ($32\text{--}250\text{ cm}^{-1}$) related to pure rotation or translation of the $[\text{PO}_4]$.^{61,65} The presence of well-defined Raman-active modes in the spectra indicates all Ag_3PO_4 powders are structurally ordered at short range. However, the more defined bands exhibited by the samples subjected to the MAH processing for 16 and 32 min can be associated with a decrease in the concentration of structural defects by the microwave radiation.

3.3. Morphological Aspects. The efficient control on the size, shape, composition, structure, and surface chemistry of any material allows modification of its physicochemical properties.⁶⁶ Hence, several researchers have tried to use many synthesis methods to modify and control the particle size and shape of Ag_3PO_4 , especially for studies focused on photocatalytic activity.^{5,15,30}

In all Ag_3PO_4 samples reported in this study, FEG-SEM micrographs revealed a high concentration of irregular spherical-like microparticles (Figure 5). These morphological aspects were maintained even after hydrothermal treatment. Based on the micrographs, a growth mechanism of these microparticles was proposed. Initially, after the formation of primary particles, they are free to rotate, randomly collide, and spontaneously rearrange in relation to one another through

Brownian motion.⁶⁷ In this stage, particle–particle interactions can occur in a common crystallographic orientation, resulting in growth by the coalescence of solid particles (oriented attachment, OA). However, when there is a small misorientation in the solid–solid interface (imperfect OA) between the particles, defects can be generated in this region (dislocations, twins, stacking faults, etc.).^{68,69} After contact, the particles can form oriented aggregates (disordered assembly) and remain irreversibly attached.⁷⁰ The junctions detected in the contact interface of Ag_3PO_4 microparticles (dotted yellow circles in Figure 5) reinforce the hypothesis of imperfect OA growth. This phenomenon appears to be more pronounced in Figure 5b–d, in which the samples were processed in MAH, i.e., under microwave irradiation. Besides local superheating, the microwave radiation accelerates the nucleation and growth processes as well as increases the effective collision rate of particles, mainly favoring their aggregation.⁷¹

The particle size average distributions for each of Ag_3PO_4 samples were statistically analyzed considering the total count of 100 microparticles by means of FE-SEM micrographs (Figure S1a–d in Supporting Information). A large variation in the average particle size distribution was observed, confirming the polydisperse nature of these particle systems. In this case, the particle sizes were (a) Ag_3PO_4 (CP), $0.30\text{ }\mu\text{m}$; (b) Ag_3PO_4 (8 min), $0.43\text{ }\mu\text{m}$; (c) Ag_3PO_4 (16 min), $0.43\text{ }\mu\text{m}$; and (d) Ag_3PO_4 (32 min), $0.52\text{ }\mu\text{m}$. This information allows the presumption that microwave radiation contributes to the particle growth during the reaction.

3.4. Growth of Metallic Silver. Figure 6 shows FEG-SEM images of Ag_3PO_4 powders before and after a 5 min exposure to the electron beam (accelerated at 15 kV) of the scanning electron microscope. The micrographs in Figure 6a,c,e,g illustrate the Ag_3PO_4 microparticles defined as time zero for each sample synthesized in this study, in which was noted the initial presence of several irregular Ag nanostructures on the surface. When these microparticles were maintained under the influence of the electron beam for 5 min (Figure 6b,d,f,h), a random and anisotropic growth of pre-existing metallic Ag nanostructures was verified, acting as active growth nuclei. The growth process occurs similarly in all samples. This behavior is new for Ag_3PO_4 powders, but it has been reported in other materials containing Ag in their compositions.^{35,37,38} Longo et al.³⁵ showed that an electron beam is able to stimulate the nucleation and growth of metallic Ag filaments on $\alpha\text{-Ag}_2\text{WO}_4$ crystals. According to these authors, the excess of electrons favored the appearance of surface defects in this tungstate, causing a continuous axial flow of Ag filaments. Another paper³⁸ reported that growth of these filaments enhances the bacteriostatic and bactericidal activities of $\alpha\text{-Ag}_2\text{WO}_4$, especially in combating to *Staphylococcus aureus*. Katsumata et al.⁷² were able to detect the presence of a metallic Ag phase in Ag_3PO_4 samples after the photodegradation experiments of bisphenol A under visible-light radiation. The appearance of Ag was explained through the reduction induced by the photo-generated electrons during the photocatalysis. Therefore, such features imply the materials containing Ag exhibit a high growth potential of irregular Ag structures on the particles.

In addition, to confirm this growth phenomenon of metallic Ag nanostructures in Ag_3PO_4 powders, an EDS system was coupled to the TEM microscope, enabling a local chemical analysis of elements in each individual microparticle. The samples were subjected to the electron beam of the TEM microscope for 5 min, in which two distinct regions (purple and

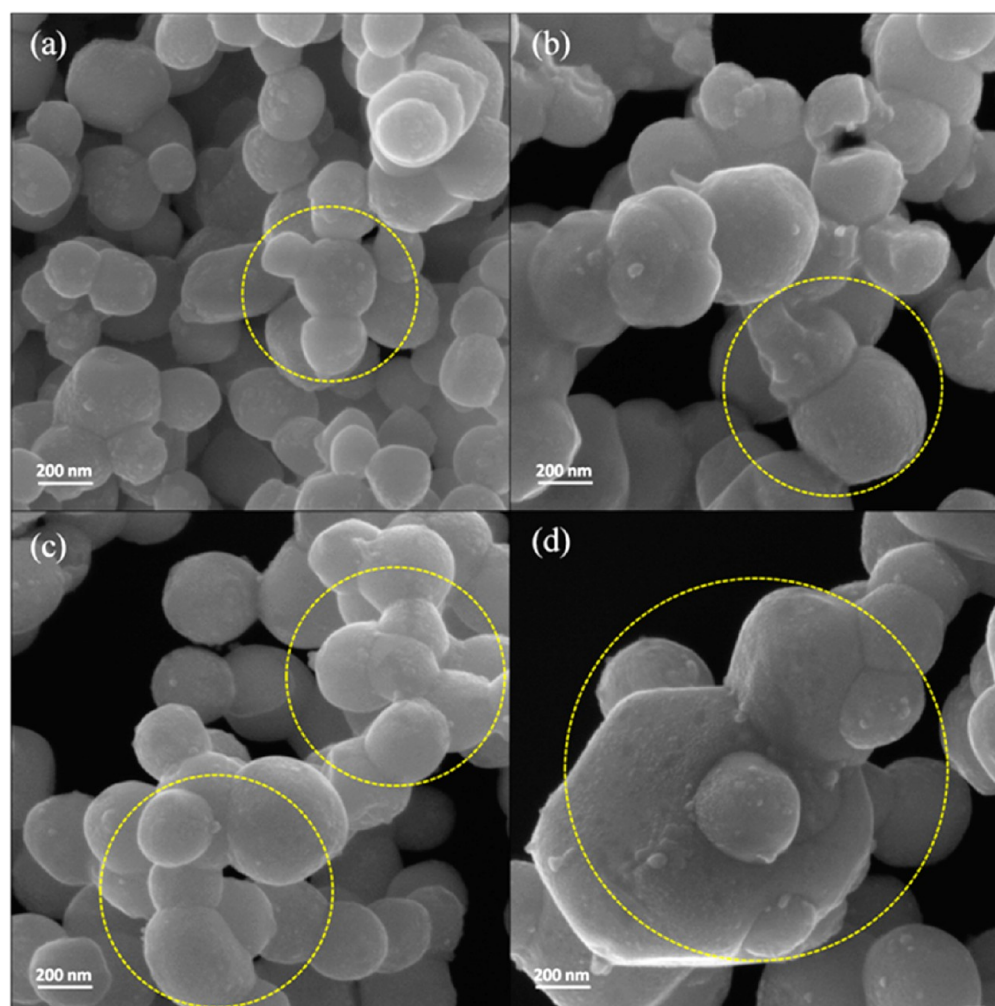


Figure 5. FEG-SEM images of Ag_3PO_4 powders synthesized by the (a) CP route and processed in a MAH system for (b) 8 min, (c) 16 min, and (d) 32 min.

green circles) in the focused microparticles were selected, as shown in Figure 7. Region 1 was chosen on an Ag growth nucleus, while region 2 was selected near the center of a single microparticle (Figure 7a,d,g,j). As expected, EDS results (Figure 7b,c,e,f,h,i,l,m) confirmed that the electrons promoted the random growth of metallic Ag nanostructures because of the large percentage of Ag atoms, especially in the microparticle region 1. In principle, these Ag atoms migrate from the matrix to the surface, resulting in structural and morphological modifications (defects). The carbon (C) and copper (Cu) atoms observed in all EDS analyses arise from the 300 mesh Cu grids used in the TEM.

3.5. Theoretical Results. Considering the experimental results reported in Figures 6 and 7, the theoretical calculations were employed to understand the phenomenon of electron absorption responsible for the growth of Ag nanostructures. For these calculations, up to five electrons were introduced into the tetrahedral $[\text{AgO}_4]$ and $[\text{PO}_4]$ clusters of cubic Ag_3PO_4 structure. The theoretically estimated values for the lattice parameters, bond lengths, and band gap energy (E_{gap}) as a function of the number of electrons (N) are shown in Table 3. The behavior of Ag–O and P–O bond lengths as a function of N is illustrated in Figure 8.

In this table, a clear increase in the lattice parameters as well as Ag–O and Ag–Ag bond lengths was observed. When the

addition of up to five electrons was taken into account in the calculations, the data revealed an increase in Ag–O bond lengths, while the P–O bond lengths remained practically constant. This behavior can be probably associated with the strong covalent character of Pb–O bonds in relation to the ionic character of Ag–O bonds. Hence, the theoretical analyses indicate the incorporation of electrons is responsible for structural modifications and formation of defects on the $[\text{AgO}_4]$ clusters, generating the ideal conditions for the growth of Ag nanostructures. It was not possible to perform an experimental analysis by means of XRD patterns and Rietveld refinements to determine the lattice parameters of Ag_3PO_4 powders after irradiation with the electron beam of FEG-SEM microscope because of the low yield of powder available with this technique.

Figure 9 shows Bader charge density of Ag, P, and O centers as a function of N . In this calculation, Ag atoms of $[\text{AgO}_4]$ clusters have a higher tendency to be reduced rather than the P atoms. Particularly at $N = 5$, all Ag atoms are almost reduced (from 0.64e to 0.02e), whereas for P atoms a constant value of the electron density is maintained (slight decrease of 0.05 units at $N = 5$). Consequently, the electron excess imposed in the material is transferred from one cluster to another through the Ag_3PO_4 lattice, so that the formation and growth processes of Ag involve adjacent $[\text{AgO}_4]$ clusters.

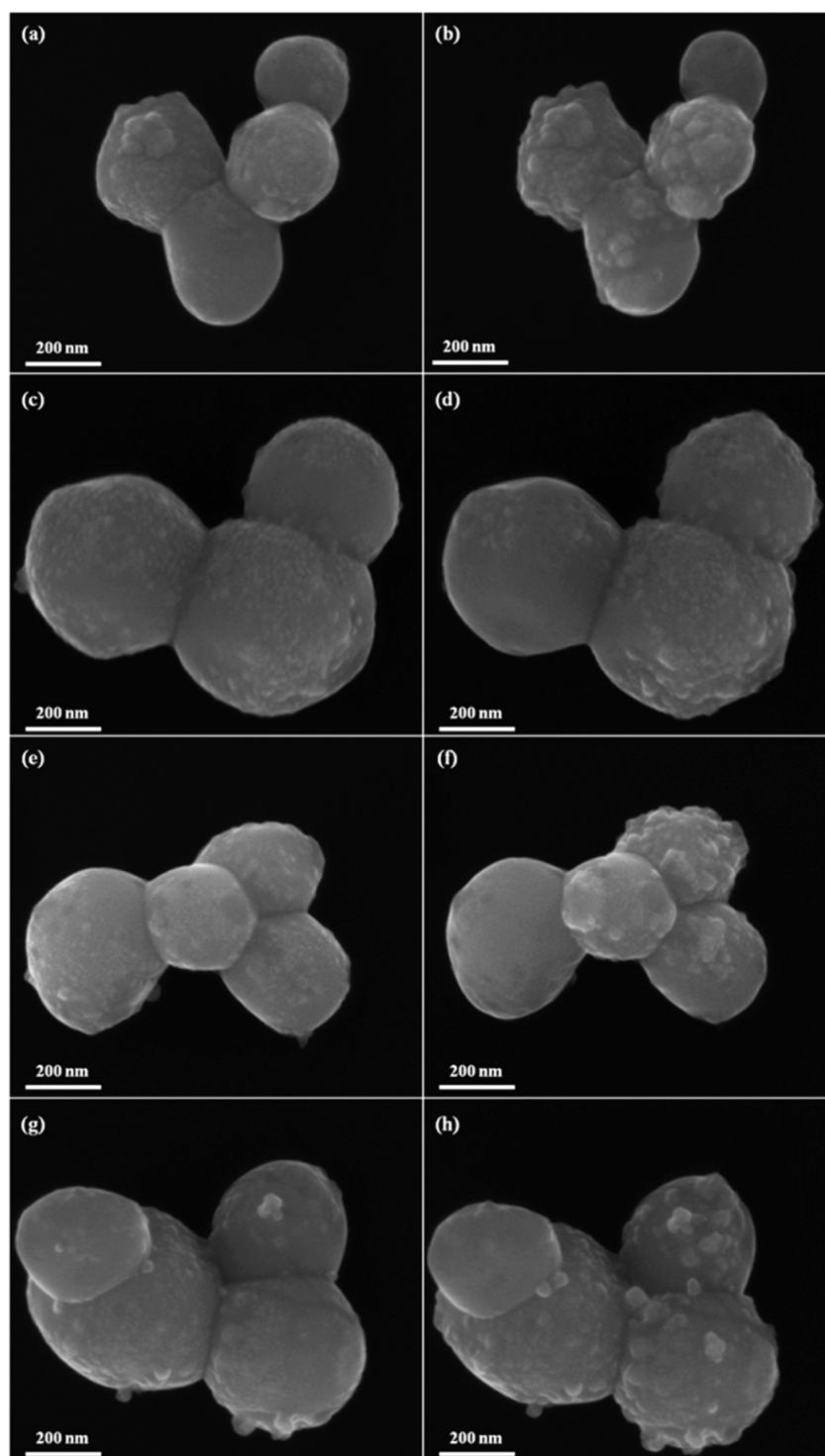


Figure 6. FEG-SEM images defined as time zero of Ag_3PO_4 powders synthesized by the (a) CP route and those processed in a MAH system for (b) 8 min, (c) 16 min, and (d) 32 min. FEG-SEM images of the same samples after 5 min of exposure to an accelerated electron beam: (e) CP and those processed in a MAH system for (d) 8 min, (f) 16 min, and (h) 32 min.

The calculations of the charge density (ρ_{bcp}) at the (3, -1) bond critical points (BCP) as well as its Laplacian ($\nabla^2\rho_{\text{bcp}}$) in Ag–O bonds of $[\text{AgO}_4]$ clusters are presented in Table 5. The addition of electrons in the material causes an interesting reduction in the theoretical ρ_{bcp} and $\nabla^2\rho_{\text{bcp}}$ values, indicating that the Ag–O bonds become less strong, favoring the formation of metallic Ag. This same behavior has been also reported in recently published papers.^{35,37}

Figure 10 shows the calculated total and projected densities of states (DOS) on atoms and orbitals as used to corroborate with the Bader charge analysis. For neutral Ag_3PO_4 ($N = 0$), the indirect E_{gap} is 2.72 eV (Table 4), which is higher than the value reported in other studies using a similar methodology, i.e., from 2.13 eV⁴⁵ to 2.36,⁵⁵ 2.43,⁷³ and 2.49 eV.⁴⁴ The DOS plots in Figure 10 are focused on the upper part of the valence band (VB) and the lower part of the conduction band (CB) of Ag

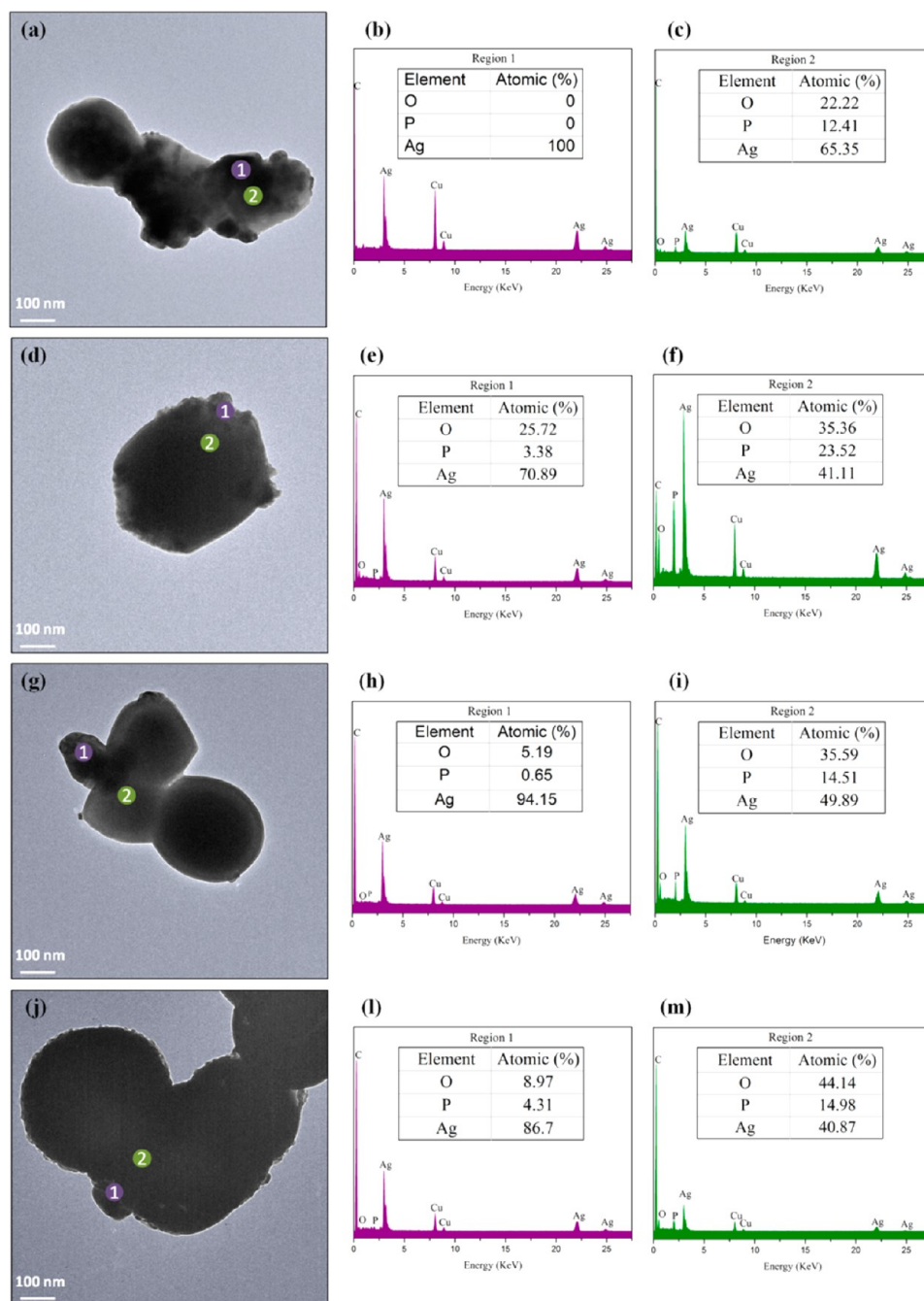


Figure 7. TEM images after 5 min of exposure to the electron beam for Ag_3PO_4 powders synthesized by the (a) CP route and those processed in a MAH system for (d) 8 min, (g) 16 min, and (j) 32 min, illustrating the two regions (purple and green circles) used in the chemical composition analysis by EDS. EDS results of Ag_3PO_4 powders synthesized by the (b,c) CP route and those processed in a MAH system for (e,f) 8 min, (h,i) 16 min, and (l,m) 32 min.

Table 3. Results Obtained by the Addition of Electrons in the Ag_3PO_4 Structure

| N | lattice parameter <i>a</i> (Å) | bond length (Å) | | | <i>E</i> _{gap} (eV) |
|---|--------------------------------|-----------------|------|-------|------------------------------|
| | | Ag–O | P–O | Ag–Ag | |
| 0 | 6.0244 | 2.37 | 1.56 | 3.01 | 2.72 |
| 1 | 6.1698 | 2.45 | 1.56 | 3.08 | 2.53 |
| 2 | 6.3107 | 2.52 | 1.56 | 3.15 | 2.30 |
| 3 | 6.4496 | 2.59 | 1.56 | 3.22 | 1.95 |
| 4 | 6.5800 | 2.66 | 1.56 | 3.29 | 1.87 |
| 5 | 6.6991 | 2.72 | 1.55 | 3.40 | 1.60 |

atoms, considering the addition of five electrons ($N = 0, 2, 3, 4$, and 5). A general analysis of the DOS shows a high contribution of *s* orbitals in the lower part of the CB for all Ag atoms. The doublet spin multiplicity is noticed for $N = 3$ and 5 , in which the α (up) and β (down) electronic contributions are not symmetric. For $N = 2$ and 4 , the spin electronic configuration is a more stable $1s$ singlet, the neutral condition of Ag_3PO_4 . The higher reduction of the E_{gap} was noted when N is 5 (Table 3). The Fermi level is placed at an energy of 0 eV. In principle, the shift of the *s* band of Ag atoms is probably caused by the interaction of the sample with the electron beam.

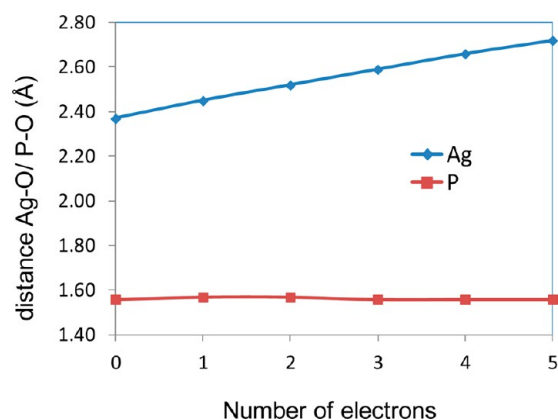


Figure 8. Ag–O and P–O bond lengths as a function of the number of electrons.

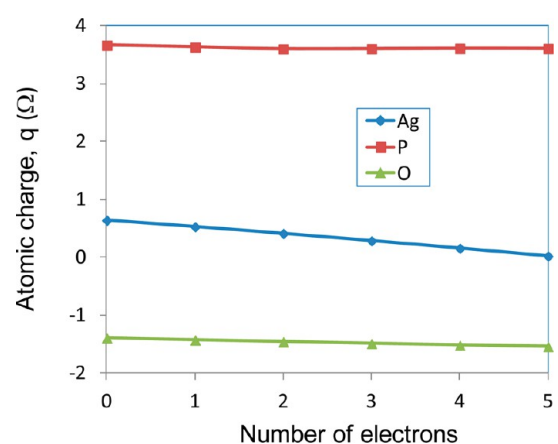


Figure 9. Bader charge density of Ag, P, and O centers for both $[\text{AgO}_4]$ and $[\text{PO}_4]$ clusters as a function of the number of electrons, where $q(\text{e})$ represents the difference between the number of valence electrons and calculated charge density.

Figure 11 shows two- and three-dimensional (2D and 3D) charge density maps associated with the interaction of $[\text{AgO}_4]$ – $[\text{PO}_4]$ clusters and $[\text{AgO}_4]$ – $[\text{AgO}_4]$ clusters, considering a neutral state ($N = 0$) and addition of five electrons ($N = 5$), respectively. The zones with high and low charge densities are specified by the concentration of charge lines around the atoms. When compared to the charge density maps of $[\text{AgO}_4]$ – $[\text{PO}_4]$ clusters in Figure 11a, the results revealed a decrease in the electronic charge density between Ag and O atoms for N from 0 to 5. Thus, the Ag–O bond lengths are enlarged because of the perturbation caused in the system with the incorporation of electrons ($N = 5$), while the P–O bond lengths remain practically constant. This behavior is probably associated with the strong covalent character of Pb–O bonds in relation to the ionic character of Ag–O bonds. In addition, the charge density maps presented in Figure 11b indicate the interactions of $[\text{AgO}_4]$ – $[\text{AgO}_4]$ clusters also become weaker when N is increased from 0 to 5, in good agreement with the Ag–Ag distances presented in Table 3. Hence, both behaviors theoretically obtained in Figure 11a,b can be associated with the growth of metallic Ag nanostructures.

3.6. Ultraviolet–Visible Absorption Spectroscopy. The E_{gap} of Ag_3PO_4 powders were experimentally estimated by extrapolating the linear portion of the UV–vis curves by means of the Kubelka–Munk (K–M) function:⁷⁴

$$F(R_{\infty}) = \frac{(1 - R_{\infty})^2}{2R_{\infty}} = \frac{K}{S} \quad (1)$$

where $F(R_{\infty})$ is the Kubelka–Munk function or absolute reflectance of the sample. In this case, magnesium oxide (MgO) was adopted as the standard sample in reflectance measurements; $R_{\infty} = R_{\text{sample}}/R_{\text{MgO}}$ (R_{∞} is the reflectance), K the molar absorption coefficient, and S the scattering coefficient. The absorption coefficient (α) of semiconductor oxides is calculated by⁷⁵

$$\alpha h\nu = C_1(h\nu - E_{\text{gap}})^n \quad (2)$$

where $h\nu$ is the photon energy, C_1 a proportionality constant, E_{gap} the band gap energy, and n a constant associated with the different types of electronic transitions. Theoretical and experimental studies have reported that Ag_3PO_4 powders exhibit indirect allowed electronic transitions;^{5,55,58–60} therefore, the condition of $n = 2$ was adopted in eq 2. When eqs 1 and 2 are combined, it is possible to obtain the modified K–M equation:⁷⁴

$$(F(R_{\infty})h\nu)^{1/2} = C_2(h\nu - E_{\text{gap}}) \quad (3)$$

Therefore, when a graph of $(F(R_{\infty})h\nu)^{1/2}$ against $h\nu$ is plotted, it is possible to determine the E_{gap} of Ag_3PO_4 powders. UV–vis spectra of all AgPO_4 powders obtained in this study are illustrated in Figure S2a–d in Supporting Information, and their respective E_{gap} values are listed in Table 5.

The structural defects have a key importance for the appearance of uncountable intermediary energy states between the VB and CB, which are commonly known as deep donors and shallow holes.⁷⁶ These defects have a direct influence on the E_{gap} of materials and, consequently, on their electronic conductivity properties.

Table 5 shows a slight increase in the E_{gap} of Ag_3PO_4 samples processed in the MAH system with respect to that obtained by the CP. It is presumed that the Ag_3PO_4 samples synthesized by the CP route favored the creation of a high density of structural defects (short, medium, and/or long range) as a response to the formation and interaction events of the microcrystals. When these samples were processed in the MAH, the microwave radiation probably caused a reduction of structural defects in the AgPO_4 matrix, increasing the E_{gap} . Moreover, the presence of uncountable kinds of defects is extremely difficult to simulate by means of theoretical calculations to justify the higher E_{gap} (2.72 eV) found in Table 3 for Ag_3PO_4 ($N = 0$).

3.7. Photoluminescence. In terms of optical phenomena, few scientific studies on the PL properties of Ag_3PO_4 powders have been reported in the literature.^{7,77,78} According to Liang et al.,⁷⁸ the origin of this physical property in this material arises from the recombination of the charge-transfer transition between O2p orbitals and empty Ag5d orbitals or is due to the self-trapped excitons in the PO_4 complex oxyanion. Thus, the main factors responsible for the PL emission of this material remain a great challenge for theoretical and experimental scientists.

Figure 12 shows PL spectra of Ag_3PO_4 powders using an excitation wavelength of 350 nm. These spectra have typical broad band profiles with the maximum emissions located in the blue region of the visible electromagnetic spectrum. Similar PL profiles were verified in Ag_2WO_4 powders processed by the MAH by Longo et al.³⁷ who explained that the blue emissions were caused by the lattice former ($[\text{WO}_6]$ clusters), while the

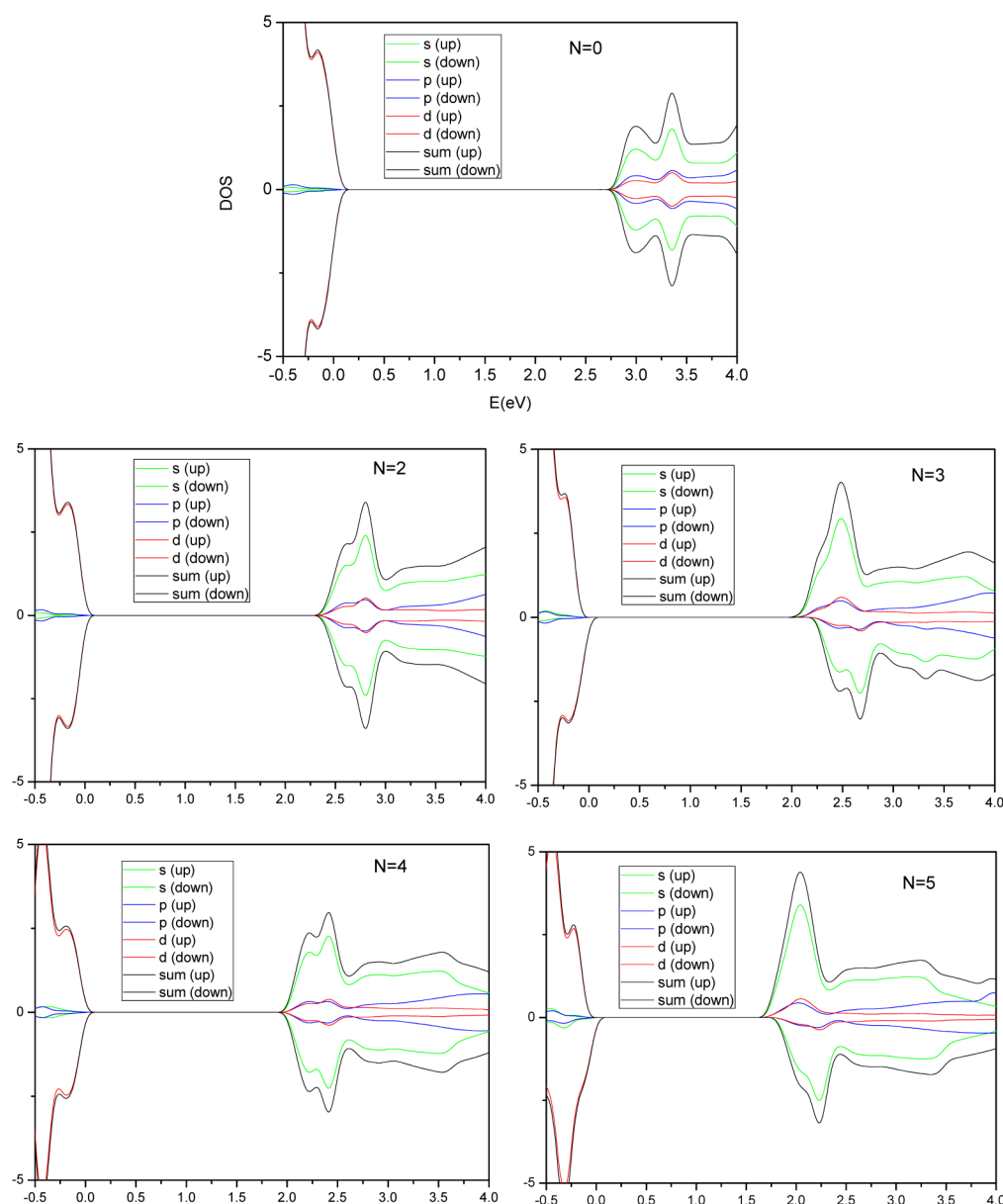


Figure 10. DOS plots analyzing the upper part of the VB and the lower part of the CB of different Ag atoms where $N = 0, 2, 3, 4$, and 5 .

Table 4. Charge Density at the $(3, -1)$ BCPs and its Laplacian in Ag–O Bonds of $[\text{AgO}_4]$ Clusters as a Function of N

| N | ρ_{bcp} | $\nabla^2 \rho_{\text{bcp}}$ |
|-----|---------------------|------------------------------|
| 0 | 0.31 | 3.85 |
| 1 | 0.27 | 3.35 |
| 2 | 0.23 | 2.91 |
| 3 | 0.20 | 2.51 |
| 4 | 0.18 | 2.17 |
| 5 | 0.16 | 1.90 |

changes found in the red emissions were related to the lattice modifier ($[\text{AgO}_y]$ clusters; $y = 2, 4, 6$, and 7). This same phenomenon have been observed in other materials containing Ag.⁷⁹

Hence, it is presumed that the maximum blue PL emission of Ag_3PO_4 powders is mainly caused by tetrahedral $[\text{PO}_4]$ clusters (lattice former), as detected in other phosphates.^{80–82} The

absence of a pronounced red PL emission can be a response to the high degree of distortion caused by $[\text{AgO}_4]$ clusters in the matrix (Figure 3) and/or affected by the growth of metallic Ag nanostructures (Figures 6 and 7).

In addition, the samples processed by MAH revealed a small red shift to higher wavelengths (453 nm) in relation to those obtained only by the CP route (447 nm). This particular behavior can be due to different distributions and organizations of intermediary energy levels within the forbidden band gap (Table 5).

Therefore, the Kröger–Vink notation⁸³ is employed based on the complex clusters model to explain the PL properties of Ag_3PO_4 powders. PL response of solids can be influenced by the concentration of different intrinsic (bulk/surface) and extrinsic (interface) defects (structural order–disorder), which are responsible for the modifications in the number of intermediary energy states within the band gap. In these energy states, after the photon absorption process, the recombination of electron–hole ($e'-h^\bullet$) pairs directly involves

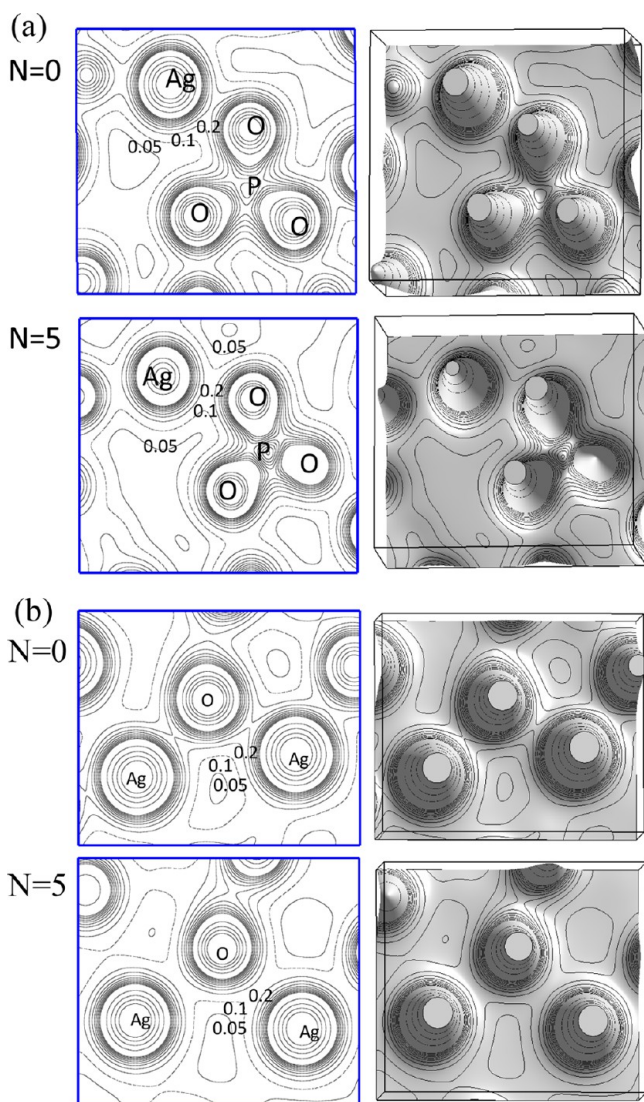


Figure 11. 2D and 3D charge density maps of (a) $[\text{AgO}_4]-[\text{PO}_4]$ clusters and (b) $[\text{AgO}_4]-[\text{AgO}_4]$ clusters for the conditions of $N = 0$ and 5.

Table 5. E_{gap} Values of Ag_3PO_4 Powders

| sample | E_{gap} (eV) |
|-----------------------------------|-----------------------|
| Ag_3PO_4 , CP | 2.16 |
| Ag_3PO_4 , 8 min | 2.23 |
| Ag_3PO_4 , 16 min | 2.20 |
| Ag_3PO_4 , 32 min | 2.25 |

a cluster-to-cluster charge transfer, i.e., between $[\text{AgO}_4]-[\text{PO}_4]$ clusters and $[\text{AgO}_4]-[\text{AgO}_4]$ clusters. Therefore, these structural defects promote a symmetry break, causing a polarization in the structure by the electronic charge transfer from ordered (o) to disordered (d) clusters (formation of $e'-h^*$ pairs). This phenomenon can be explained by the following equations:

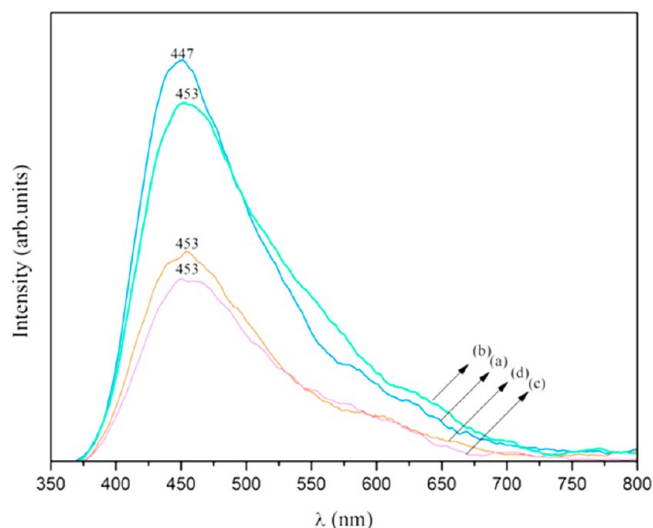
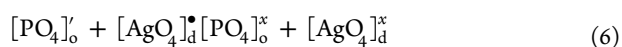
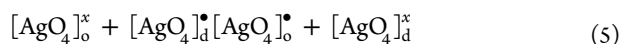
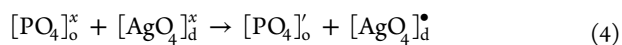


Figure 12. PL spectra of Ag_3PO_4 powders synthesized by the (a) CP route and those processed in a MAH system for (b) 8 min, (c) 16 min, and (d) 32 min.

In these equations, the superscript x indicates neutral clusters, \bullet the cluster with one hole (h^*), and $'$ the cluster with one electron (e').

Equation 4 shows formation of $e'-h^*$ pairs in the Ag_3PO_4 lattice due to the interaction of symmetric $[\text{PO}_4]_o^x$ and asymmetric $[\text{AgO}_4]_d^x$ clusters (neutral clusters). The interaction involving only $[\text{AgO}_4]$ clusters results in an electronic transfer from one cluster to another, acting as a PL suppressor (eq 5). This same suppression phenomenon occurs in eq 6, in which the $[\text{PO}_4]_o'$ clusters (donor) transfer their electrons to $[\text{AgO}_4]_d^{\bullet}$ clusters (acceptor), resulting in neutral clusters (not effective for PL).

4. CONCLUSIONS

In summary, Ag_3PO_4 powders were obtained by the CP route and subjected to the MAH treatment. X-ray diffraction and Rietveld refinements confirmed these powders have a body-centered cubic structure, in which the $[\text{AgO}_4]$ clusters are highly distorted in relation to regular $[\text{PO}_4]$ clusters. The presence of vibrational bands in all Raman spectra revealed the Ag_3PO_4 is locally ordered; it is independent of the processing temperature employed in the MAH. In morphological terms, Ag_3PO_4 is composed of several irregular spherical-like microparticles containing metallic Ag nanostructures on the surface. The random growth of these nanostructures was stimulated with the electron beam during the irradiation; therefore, a structural disorder was introduced in the material. When up to five electrons were taken into account in the theoretical calculations, a pronounced modification in the Ag–O bond lengths of $[\text{AgO}_4]$ clusters was detected, suggesting that the incorporation of electrons induces the growth of Ag in the microparticles. When the E_{gap} values were compared, the results demonstrated the microwave radiation in the MAH is able to reduce the presence of intermediary energy states within the band gap. Maximum PL emissions of all samples were observed in the region of visible blue light, indicating a high contribution of $[\text{PO}_4]$ clusters.

■ ASSOCIATED CONTENT

■ Supporting Information

Atomic coordinates obtained from Rietveld refinements of Ag_3PO_4 powders synthesized by the CP route and those processed in a MAH system (Table S1); bond angles and lengths of $[\text{AgO}_4]$ and $[\text{PO}_4]$ clusters (Table S2); average particle size distribution of Ag_3PO_4 powders synthesized by the CP route and those processed in a MAH system (Figure S1); UV-vis spectra of Ag_3PO_4 powders synthesized by the CP route and those processed in a MAH system (Figure S2); TEM images of Ag_3PO_4 powders (Figure S3). This material is available free of charge via the Internet at <http://pubs.acs.org>.

■ AUTHOR INFORMATION

Notes

The authors declare no competing financial interest.

■ ACKNOWLEDGMENTS

The authors are grateful to Prometeo/2009/053 (Generalitat Valenciana), Ministerio de Economía y Competitividad (Spain), CTQ2012-36253-C03-02, Spanish Brazilian program (PHB2009-0065-PC), CAPES (203038 009607/2013-56), INCTMN (2008/57872-1), FAPESP (2012/14004-5; 2013/07296-2), CNPq (147001/2013-7; 573636/2008-7) for financially supporting this research. We also acknowledge the Servei Informàtica, Universitat Jaume I, for the generous allotment of computer time.

■ REFERENCES

- (1) Masse, R.; Tordjman, I.; Durif, A. Refinement of Crystal - Structure of Silver Monophosphate, Ag_3PO_4 - Existence of High-Temperature Form. *Z. Kristallogr., Kristallgeom., Kristallphys., Kristallchem.* **1976**, *144*, 76–81.
- (2) Yi, Z.; Withers, R. L.; Liu, Y. A Two-Step Approach Towards Solar-Driven Water Splitting. *Electrochem. Commun.* **2011**, *13*, 28–30.
- (3) Yi, Z.; et al. An Orthophosphate Semiconductor with Photooxidation Properties under Visible-Light Irradiation. *Nat. Mater.* **2010**, *9*, 559–564.
- (4) Bi, Y.; Hu, H.; Ouyang, S.; Lu, G.; Cao, J.; Ye, J. Photocatalytic and Photoelectric Properties of Cubic Ag_3PO_4 Sub-Microcrystals with Sharp Corners and Edges. *Chem. Commun. (Cambridge, U.K.)* **2012**, *48*, 3748–3750.
- (5) Bi, Y.; Ouyang, S.; Umezawa, N.; Cao, J.; Ye, J. Facet Effect of Single-Crystalline Ag_3PO_4 Sub-Microcrystals on Photocatalytic Properties. *J. Am. Chem. Soc.* **2011**, *133*, 6490–6492.
- (6) Wang, W.; Cheng, B.; Yu, J.; Liu, G.; Fan, W. Visible-Light Photocatalytic Activity and Deactivation Mechanism of Ag_3PO_4 Spherical Particles. *Chem.—Asian J.* **2012**, *7*, 1902–1908.
- (7) Kumar, S.; Surendar, T.; Shanker, V. Template-Free and Eco-Friendly Synthesis of Hierarchical Ag_3PO_4 Microcrystals with Sharp Corners and Edges for Enhanced Photocatalytic Activity under Visible Light. *Mater. Lett.* **2014**, *123*, 172–175.
- (8) Cao-Thang, D.; Thanh-Dinh, N.; Kleitz, F.; Trong-On, D. Large-Scale Synthesis of Uniform Silver Orthophosphate Colloidal Nanocrystals Exhibiting High Visible Light Photocatalytic Activity. *Chem. Commun. (Cambridge, U.K.)* **2011**, *47*, 7797–7799.
- (9) Khan, A.; Qamar, M.; Muneer, M. Synthesis of Highly Active Visible-Light-Driven Colloidal Silver Orthophosphate. *Chem. Phys. Lett.* **2012**, *519–520*, 54–58.
- (10) Liang, Q.; Ma, W.; Shi, Y.; Li, Z.; Yang, X. Hierarchical Ag_3PO_4 Porous Microcubes with Enhanced Photocatalytic Properties Synthesized with the Assistance of Trisodium Citrate. *CrystEngComm* **2012**, *14*, 2966.
- (11) Liu, Y.; Fang, L.; Lu, H.; Li, Y.; Hu, C.; Yu, H. One-Pot Pyridine-Assisted Synthesis of Visible-Light-Driven Photocatalyst $\text{Ag}/\text{Ag}_3\text{PO}_4$. *Appl. Catal., B* **2012**, *115–116*, 245–252.
- (12) Wang, J.; Teng, F.; Chen, M.; Xu, J.; Song, Y.; Zhou, X. Facile Synthesis of Novel Ag_3PO_4 Tetrapods and the {110} Facets-Dominated Photocatalytic Activity. *CrystEngComm* **2013**, *15*, 39.
- (13) Wang, K.; Xu, J.; Hua, X.; Li, N.; Chen, M.; Teng, F.; Zhu, Y.; Yao, W. Highly Efficient Photodegradation of RhB–MO Mixture Dye Wastewater by Ag_3PO_4 Dodecahedrons under Acidic Condition. *J. Mol. Catal. A: Chem.* **2014**, *393*, 302–308.
- (14) Yang, X.; Qin, J.; Jiang, Y.; Li, R.; Li, Y.; Tang, H. Bifunctional $\text{TiO}_2/\text{Ag}_3\text{PO}_4$ /Graphene Composites with Superior Visible Light Photocatalytic Performance and Synergistic Inactivation of Bacteria. *RSC Adv.* **2014**, *4*, 18627–18636.
- (15) Wang, J.; Lou, S.; Sun, P.; Wang, L.; Teng, Y.; Chen, M.; Teng, F. Surface Control and Photocatalytic Activity of Branched Silver Orthophosphate Dendrites. *ChemCatChem* **2014**, *6*, 2021–2027.
- (16) Yao, W.; Zhang, B.; Huang, C.; Ma, C.; Song, X.; Xu, Q. Synthesis and Characterization of High Efficiency and Stable $\text{Ag}_3\text{PO}_4/\text{TiO}_2$ Visible Light Photocatalyst for the Degradation of Methylene Blue and Rhodamine B Solutions. *J. Mater. Chem.* **2012**, *22*, 4050–4055.
- (17) Rawal, S. B.; Sung, S. D.; Lee, W. I. Novel $\text{Ag}_3\text{PO}_4/\text{TiO}_2$ Composites for Efficient Decomposition of Gaseous 2-Propanol under Visible-Light Irradiation. *Catal. Commun.* **2012**, *17*, 131–135.
- (18) Teng, W.; Li, X.; Zhao, Q.; Chen, G. Fabrication of $\text{Ag}/\text{Ag}_3\text{PO}_4/\text{TiO}_2$ Heterostructure Photoelectrodes for Efficient Decomposition of 2-Chlorophenol under Visible Light Irradiation. *J. Mater. Chem. A* **2013**, *1*, 9060–9068.
- (19) Bi, Y.; Hu, H.; Ouyang, S.; Jiao, Z.; Lu, G.; Ye, J. Selective Growth of Metallic Ag Nanocrystals on Ag_3PO_4 Submicro-Cubes for Photocatalytic Applications. *Chem.—Eur. J.* **2012**, *18*, 14272–14275.
- (20) Teng, W.; Li, X.; Zhao, Q.; Zhao, J.; Zhang, D. In Situ Capture of Active Species and Oxidation Mechanism of RhB and MB Dyes over Sunlight-Driven $\text{Ag}/\text{Ag}_3\text{PO}_4$ Plasmonic Nanocatalyst. *Appl. Catal., B* **2012**, *125*, 538–545.
- (21) Bi, Y.; Hu, H.; Ouyang, S.; Jiao, Z.; Lu, G.; Ye, J. Selective Growth of Ag_3PO_4 Submicro-Cubes on Ag Nanowires to Fabricate Necklace-Like Heterostructures for Photocatalytic Applications. *J. Mater. Chem.* **2012**, *22*, 14847–14850.
- (22) Li, G.; Mao, L. Magnetically Separable $\text{Fe}_3\text{O}_4\text{-Ag}_3\text{PO}_4$ Sub-Micrometre Composite: Facile Synthesis, High Visible Light-Driven Photocatalytic Efficiency, and Good Recyclability. *RSC Adv.* **2012**, *2*, 5108–5111.
- (23) Bi, Y.; Ouyang, S.; Cao, J.; Ye, J. Facile Synthesis of Rhombic Dodecahedral $\text{AgX}/\text{Ag}_3\text{PO}_4$ ($\text{X} = \text{Cl}, \text{Br}, \text{I}$) Heterocrystals with Enhanced Photocatalytic Properties and Stabilities. *Phys. Chem. Chem. Phys.* **2011**, *13*, 10071–10075.
- (24) Chen, X.; Huang, X.; Yi, Z. Enhanced Ethylene Photodegradation Performance of $\text{g-C}_3\text{N}_4\text{-Ag}_3\text{PO}_4$ Composites with Direct Z-Scheme Configuration. *Chem.—Eur. J.* **2014**, *1–8*.
- (25) Tennakone, K.; Jayatissa, A. H.; Wijeratne, W. Photocleavage of Water with Silver Phosphate. *J. Chem. Soc., Chem. Commun.* **1988**, 496–498.
- (26) Rotello, V. *Nanoparticles: Building Blocks for Nanotechnology*; Springer Science Business Media Inc: New York, 2004; p 284.
- (27) Sattler, K. D. *Handbook of Nanophysics: Nanoparticles and Quantum Dots*; CRC Press: New York, 2010; p 716.
- (28) Wu, A.; Tian, C.; Chang, W.; Hong, Y.; Zhang, Q.; Qu, Y.; Fu, H. Morphology-Controlled Synthesis of Ag_3PO_4 Nano/Microcrystals and Their Antibacterial Properties. *Mater. Res. Bull.* **2013**, *48*, 3043–3048.
- (29) Liu, J.-K.; Luo, C.-X.; Wang, J.-D.; Yang, X.-H.; Zhong, X.-H. Controlled Synthesis of Silver Phosphate Crystals with High Photocatalytic Activity and Bacteriostatic Activity. *CrystEngComm* **2012**, *14*, 8714–8721.
- (30) Que, R. High-Yield Synthesized Silver Orthophosphate Nanowires and Their Application in Photoswitch. *Front. Optoelectron.* **2011**, *4*, 176–180.
- (31) Komarneni, S.; Roy, R.; Li, Q. H. Microwave-Hydrothermal Synthesis of Ceramic Powders. *Mater. Res. Bull.* **1992**, *27*, 1393–1405.

- (32) Komarneni, S.; Menon, V. C. Hydrothermal and Microwave-Hydrothermal Preparation of Silica Gels. *Mater. Lett.* **1996**, *27*, 313–315.
- (33) Komarneni, S.; Rajha, R. K.; Katsuki, H. Microwave-Hydrothermal Processing of Titanium Dioxide. *Mater. Chem. Phys.* **1999**, *61*, 50–54.
- (34) Leadbeater, N. E. *Microwave Heating as a Tool for Sustainable Chemistry*; CRC Press: Boca Raton, FL, 2010; p 290.
- (35) Longo, E.; Cavalcante, L. S.; Volanti, D. P.; Gouveia, A. F.; Longo, V. M.; Varela, J. A.; Orlandi, M. O.; Andres, J. Direct in Situ Observation of the Electron-Driven Synthesis of Ag Filaments on α - Ag_2WO_4 Crystals. *Sci. Rep.* **2013**, *3*, 1–4.
- (36) Andrés, J.; et al. Structural and Electronic Analysis of the Atomic Scale Nucleation of Ag on α - Ag_2WO_4 Induced by Electron Irradiation. *Sci. Rep.* **2014**, *4*, 1–7.
- (37) Longo, E.; Volanti, D. P.; Longo, V. M.; Gracia, L.; Nogueira, I. C.; Almeida, M. A. P.; Pinheiro, A. N.; Ferrer, M. M.; Cavalcante, L. S.; Andrés, J. Toward an Understanding of the Growth of Ag Filaments on α - Ag_2WO_4 and Their Photoluminescent Properties: A Combined Experimental and Theoretical Study. *J. Phys. Chem. C* **2014**, *118*, 1229–1239.
- (38) Longo, V. M.; et al. Potentiated Electron Transference in α - Ag_2WO_4 Microcrystals with Ag Nanofilaments as Microbial Agent. *J. Phys. Chem. A* **2014**, *118*, 5769–5778.
- (39) Longo, E.; Varela, J. A.; Almeida, D. K.; Volanti, D. P. Microwave Aided Device for Hydrothermal Synthesis of Nanostructured Oxides, Particularly Obtaining Particles of Metal Oxides, Comprises Container, in Which Hydrothermal Reaction Takes Place, and Lid for Container. BR200815393-A2, December 07, 2010.
- (40) Kresse, G.; Furthmüller, J. Efficiency of Ab-Initio Total Energy Calculations for Metals and Semiconductors Using a Plane-Wave Basis Set. *Comput. Mater. Sci.* **1996**, *6*, 15–50.
- (41) Kresse, G.; Hafner, J. Ab-Initio Molecular-Dynamics Simulation of the Liquid-Metal Amorphous-Semiconductor Transition in Germanium. *Phys. Rev. B: Condens. Matter Mater. Phys.* **1994**, *49*, 14251–14269.
- (42) Heyd, J.; Scuseria, G. E.; Ernzerhof, M. Hybrid Functionals Based on a Screened Coulomb Potential. *J. Chem. Phys.* **2003**, *118*, 8207–8215.
- (43) Krukau, A. V.; Vydrov, O. A.; Izmaylov, A. F.; Scuseria, G. E. Influence of the Exchange Screening Parameter on the Performance of Screened Hybrid Functionals. *J. Chem. Phys.* **2006**, *125*, 224106.
- (44) Reunchan, P.; Umezawa, N. Native Defects and Hydrogen Impurities in Ag_3PO_4 . *Phys. Rev. B: Condens. Matter Mater. Phys.* **2013**, *87*, 245205.
- (45) Kahl, J. M.; Sheridan, D. L.; Kehoe, A. B.; Scanlon, D. O.; Morgan, B. J.; Watson, G. W.; Payne, D. J. The Electronic Structure of Silver Orthophosphate: Experiment and Theory. *J. Mater. Chem. A* **2014**, *2*, 6092–6099.
- (46) Kresse, G.; Joubert, D. From Ultrasoft Pseudopotentials to the Projector Augmented-Wave Method. *Phys. Rev. B: Condens. Matter Mater. Phys.* **1999**, *59*, 1758–1775.
- (47) Perdew, J. P.; Burke, K.; Ernzerhof, M. Generalized Gradient Approximation Made Simple. *Phys. Rev. Lett.* **1996**, *77*, 3865–3868.
- (48) Bader, R. F. W. *Atoms in Molecules: A Quantum Theory*; Clarendon Press: Oxford New York, 1990; p 438.
- (49) Hohenberg, P.; Kohn, W. Inhomogeneous Electron Gas. *Phys. Rev.* **1964**, *136*, B864–B870.
- (50) Popelier, P. L. A. *Atoms in Molecules: An Introduction*; Prentice Hall: Harlow, U.K., 2000; p 164.
- (51) Matta, C. F.; Boyd, R. J. *The Quantum Theory of Atoms in Molecules: From Solid State to DNA and Drug Design*; Wiley-VCH: Weinheim, Germany, 2007; p 567.
- (52) Rietveld, H. M. A Profile Refinement Method for Nuclear and Magnetic Structures. *J. Appl. Crystallogr.* **1969**, *2*, 65–71.
- (53) Toby, B. H. EXPGUI, a Graphical User Interface for GSAS. *J. Appl. Crystallogr.* **2001**, *34*, 210–213.
- (54) Finger, L. W.; Cox, D. E.; Jephcoat, A. P. A Correction for Powder Diffraction Peak Asymmetry Due to Axial Divergence. *J. Appl. Crystallogr.* **1994**, *27*, 892–900.
- (55) Ma, X.; Lu, B.; Li, D.; Shi, R.; Pan, C.; Zhu, Y. Origin of Photocatalytic Activation of Silver Orthophosphate from First-Principles. *J. Phys. Chem. C* **2011**, *115*, 4680–4687.
- (56) Rosa, I. L. V.; Marques, A. P. A.; Tanaka, M. T. S.; Melo, D. M. A.; Leite, E. R.; Longo, E.; Arana Varela, J. Synthesis, Characterization and Photophysical Properties of Eu^{3+} Doped in BaMoO_4 . *J. Fluoresc.* **2008**, *18*, 239–245.
- (57) Marques, A. P. A.; Picon, F. C.; Melo, D. M. A.; Pizani, P. S.; Leite, E. R.; Varela, J. A.; Longo, E. Effect of the Order and Disorder of BaMoO_4 Powders in Photoluminescent Properties. *J. Fluoresc.* **2008**, *18*, 51–59.
- (58) Dong, P.; Wang, Y.; Cao, B.; Xin, S.; Guo, L.; Zhang, J.; Li, F. Ag_3PO_4 /Reduced Graphite Oxide Sheets Nanocomposites with Highly Enhanced Visible Light Photocatalytic Activity and Stability. *Appl. Catal., B* **2013**, *132*, 45–53.
- (59) Cheng, L.-W.; Tsai, J.-C.; Huang, T.-Y.; Huang, C.-W.; Unnikrishnan, B.; Lin, Y.-W. Controlled Synthesis, Characterization and Photocatalytic Activity of BiPO_4 Nanostructures with Different Morphologies. *Mater. Res. Express* **2014**, *1*, 1–19.
- (60) Mroczkowska, M.; Nowinski, J. L.; Zukowska, G. Z.; Mroczkowska, A.; Garbacz, J. E.; Wasiluk, M.; Gierlotka, S. Micro Raman, FT-IR/PAS, XRD and SEM Studies on Glassy and Partly Crystalline Silver Phosphate Ionic Conductors. *J. Power Sources* **2007**, *173*, 729–733.
- (61) Liu, B.; Li, Z.; Xu, S.; Han, D.; Lu, D. Enhanced Visible-Light Photocatalytic Activities of Ag_3PO_4 /MWCNT Nanocomposites Fabricated by Facile in Situ Precipitation Method. *J. Alloys Compd.* **2014**, *596*, 19–24.
- (62) Cui, C.; Wang, Y.; Liang, D.; Cui, W.; Hu, H.; Lu, B.; Xu, S.; Li, X.; Wang, C.; Yang, Y. Photo-Assisted Synthesis of Ag_3PO_4 /Reduced Graphene Oxide/Ag Heterostructure Photocatalyst with Enhanced Photocatalytic Activity and Stability under Visible Light. *Appl. Catal., B* **2014**, *158–159*, 150–160.
- (63) Preston, C. M.; Adams, W. A.; Laser Raman, A. Spectroscopic Study of Aqueous Orthophosphate Salts. *J. Phys. Chem.* **1979**, *83*, 814–821.
- (64) Tuschel, D. Practical Group Theory and Raman Spectroscopy, Part II: Application of Polarization. *Spectroscopy* **2014**, *29*, 14–23.
- (65) Turkovi, A.; Fox, D. L.; Scott, J. F.; Geller, S.; Ruse, G. F. High Temperature Raman Spectroscopy of Silver Tetratungstate. *Mater. Res. Bull.* **1977**, *12*, 189–196.
- (66) Thanh-Dinh, N. From Formation Mechanisms to Synthetic Methods Toward Shape-Controlled Oxide Nanoparticles. *Nanoscale* **2013**, *5*, 9455–9482.
- (67) Penn, R. L.; Soltis, J. A. Characterizing Crystal Growth by Oriented Aggregation. *CrystEngComm* **2014**, *16*, 1409–1418.
- (68) Penn, R. L.; Banfield, J. F. Imperfect Oriented Attachment: Dislocation Generation in Defect-Free Nanocrystals. *Science* **1998**, *281*, 969–971.
- (69) Penn, R. L.; Banfield, J. F. Oriented Attachment and Growth, Twinning, Polytypism, and Formation of Metastable Phases: Insights from Nanocrystalline TiO_2 . *Am. Mineral.* **1998**, *83*, 1077–1082.
- (70) Dalmascio, C. J.; Ribeiro, C.; Leite, E. R. Impact of the Colloidal State on the Oriented Attachment Growth Mechanism. *Nanoscale* **2010**, *2*, 2336–2345.
- (71) Bilecka, I.; Niederberger, M. Microwave Chemistry for Inorganic Nanomaterials Synthesis. *Nanoscale* **2010**, *2*, 1358–1374.
- (72) Katsumata, H.; Taniguchi, M.; Kaneko, S.; Suzuki, T. Photocatalytic Degradation of Bisphenol A by Ag_3PO_4 under Visible Light. *Catal. Commun.* **2013**, *34*, 30–34.
- (73) Liu, J. J.; Fu, X. L.; Chen, S. F.; Zhu, Y. F. Electronic Structure and Optical Properties of Ag_3PO_4 Photocatalyst Calculated by Hybrid Density Functional Method. *Appl. Phys. Lett.* **2011**, *99*, 191903.
- (74) Tolvaj, L.; Mitsui, K.; Varga, D. Validity Limits of Kubelka–Munk Theory for Drift Spectra of Photodegraded Solid Wood. *Wood Sci. Technol.* **2011**, *45*, 135–146.

- (75) Wood, D. L.; Tauc, J. Weak Absorption Tails in Amorphous Semiconductors. *Phys. Rev. B: Solid State* **1972**, *5*, 3144–3151.
- (76) Lyons, J. L.; Janotti, A.; Van de Walle, C. G. Shallow Versus Deep Nature of Mg Acceptors in Nitride Semiconductors. *Phys. Rev. Lett.* **2012**, *108*, 1564403.
- (77) Ge, M.; Zhu, N.; Zhao, Y.; Li, J.; Liu, L. Sunlight-Assisted Degradation of Dye Pollutants in Ag_3PO_4 Suspension. *Ind. Eng. Chem. Res.* **2012**, *51*, 5167–5173.
- (78) Liang, Q.; Shi, Y.; Ma, W.; Li, Z.; Yang, X. Enhanced Photocatalytic Activity and Structural Stability by Hybridizing Ag_3PO_4 Nanospheres with Graphene Oxide Sheets. *Phys. Chem. Chem. Phys.* **2012**, *14*, 15657–15665.
- (79) Gouveia, A. F.; Sczancoski, J. C.; Ferrer, M. M.; Lima, A. S.; Santos, M. R.; Li, M. S.; Santos, R. S.; Longo, E.; Cavalcante, L. S. Experimental and Theoretical Investigations of Electronic Structure and Photoluminescence Properties of $\beta\text{-Ag}_2\text{MoO}_4$ Microcrystals. *Inorg. Chem.* **2014**, *53*, 5589–5599.
- (80) Ekthammathat, N.; Thongtem, T.; Phuruangrat, A.; Thongtem, S. Facile Hydrothermal Synthesis and Optical Properties of Monoclinic CePO_4 Nanowires with High Aspect Ratio. *J. Nano Mater.* **2012**, *2012*, 1–6.
- (81) Phuruangrat, A.; Ekthammathat, N.; Thongtem, S.; Thongtem, T. Preparation of LaPO_4 Nanowires with High Aspect Ratio by a Facile Hydrothermal Method and Their Photoluminescence. *Res. Chem. Intermed.* **2012**, *39*, 1363–1371.
- (82) Guan, M.; Sun, J.; Tao, F.; Xu, Z. A Host Crystal for the Rare-Earth Ion Dopants: Synthesis of Pure and Ln-Doped Urchinlike BiPO_4 Structure and Its Photoluminescence. *Cryst. Growth Des.* **2008**, *8*, 2694–2697.
- (83) Kröger, F. A.; Vink, H. J. Relations between the Concentrations of Imperfections in Crystalline Solids. *Solid State Phys.* **1956**, *3*, 307–435.